Open Access | Vita

Structural basis for the assembly and modulation of human M-channels

Fangzhou Lu[1,2#], Xiaoshuang Huang[1#], Guanxing Cai[3#], Xianglong Shen[1,2], Yuzhen Xie[1], Pei Huang[1,2], Feifan Yu[1,2], Xiao Fan[*1], Jian Huang[*1]

Human M-channels, primarily assembled by heteromeric KCNQ2/KCNQ3 subunits, are critical regulators of neuronal excitability, and loss-of-function mutations in either subunit are linked to epileptic disorders. Yet, the molecular mechanisms underlying heteromeric assembly, gating, and pharmacological modulation have remained largely elusive. Here, we present high-resolution cryo-EM structures of human M-channels in *apo* and activator-bound states, revealing a dominant asymmetric 3:1 and a minor staggered 2:2 stoichiometry of KCNQ2 to KCNQ3, with consistent ratios across datasets. We further examine the mechanisms of action of two distinct modulators: ICA-110381 selectively engages and stabilizes activated KCNQ2 voltage sensors, whereas XEN1101 occupies pore fenestrations and promotes channel opening through a PIP_2-assisted cooperative gating process. Electrophysiological analyses corroborate these observations, establishing the basis for subtype-selective modulation, cooperative gating, and KCNQ3-driven low-voltage activation. Together, our findings provide a foundation for interpreting pathogenic mutations and advancing the rational design of next-generation antiepileptic therapeutics targeting the M-channels.

https://doi.org/10.15302/vita.2026.05.0035

INTRODUCTION

Voltage-gated potassium channels of the KCNQ family (KCNQ1–5) are widely expressed in excitable tissues, where they shape action potentials by driving repolarization and stabilizing the membrane potential[1-3]. Individual isoforms exhibit distinct tissue distributions: KCNQ1 predominates in the heart, kidney, and cochlea[2,4], KCNQ4 is restricted to inner ear hair cells and certain brainstem regions involved in auditory modulation[5,6], and KCNQ2, KCNQ3 and KCNQ5 are enriched in the central nervous system[1,7-9]. Among neuronal channels, KCNQ2 and KCNQ3 form homo- and hetero-tetramers that primarily mediate the slowly activating, non-inactivating M-current, a key regulator of neuronal excitability at the axon initial segment and nodes of Ranvier[9-14]. Notably, heteromeric KCNQ2/KCNQ3 channels generate substantially larger currents than either homomer, highlighting their crucial physiological and therapeutic relevance[10,12,13,15].

Structurally, KCNQ channels adopt a canonical domain-swapped architecture with four independent subunits, each containing six transmembrane helices (S1–S6). The S5 and S6 segments from all subunits assemble into the central pore domain (PD), while S1–S4 constitute the peripheral voltage-sensing domains (VSDs)[2,16-19]. Recent cryo-electron microscopy (cryo-EM) studies have resolved several homomers, including KCNQ1, KCNQ2, KCNQ4, and KCNQ5[20-27], and uncovered modulatory roles for auxiliary subunits such as KCNE1/3[4,18,28,29], the chaperone calmodulin (CaM)[17,30-32], the endogenous lipid phosphatidylinositol 4,5-bisphosphate (PIP_2)[23,27,33,34], and a range of pharmacological agents[20-27,35,36]. By contrast, the structural organization and pharmacological modulation of heteromeric M-channels, especially the physiologically dominant KCNQ2/KCNQ3 complex, remain poorly understood.

Loss-of-function mutations in KCNQ2 or KCNQ3 are associated with certain types of epileptic disorders, including KCNQ2-related developmental and epileptic encephalopathy (DEE7)[37,38] and benign familial neonatal seizures (BFNS1/2)[39-41]. More than 80 pathogenic variants have been identified, underlining the critical role of M-channels in maintaining cortical excitability[30,42,43]. Enhancing the M-current pharmacologically has long been pursued for epilepsy treatment. Retigabine, the first FDA-approved KCNQ channel opener, effectively potentiated M-channel activity but was ultimately withdrawn due to adverse effects such as retinal pigmentation and urinary retention[44-46]. These liabilities were attributed to metabolism-related issues and unintended activation of retinal and bladder KCNQ isoforms[47-49], emphasizing the need for optimized chemical scaffolds and improved subtype selectivity to minimize off-target effects.

Recent efforts have yielded promising next-generation KCNQ modulators with improved specificity and safety profiles. XEN1101 (Azetukalner), a pore-targeting KCNQ2/3 channel opener, has demonstrated sustained seizure-reducing efficacy in phase III trials, without requiring titration or causing pigmentary abnormalities[50-52]. ICA-110381, by contrast, is a KCNQ2-specific activator with anticonvulsant properties that targets voltage sensors, providing a mechanistically distinct route to channel opening[22,53]. Concurrently, drug repurposing efforts have highlighted variant- and

---

1. Institute of Bio-Architecture and Bio-Interactions (IBABI), Shenzhen Medical Academy of Research and Translation (SMART), Shenzhen, Guangdong, China. 2. Westlake University, Hangzhou, Zhejiang, China. 3. Biomedical Electrophysiology Core Facility, Shenzhen Medical Academy of Research and Translation (SMART), Shenzhen, Guangdong, China. #These authors contributed equally. *Correspondence: Xiao Fan (xfan@smart.org.cn), Jian Huang (huangjian@smart.org.cn)

Received: December 1, 2025; Accepted: May 18, 2026; Published: May 27, 2026

isoform-specific effects of compounds such as gabapentin and donepezil on KCNQ channels[36,54], reinforcing the therapeutic potential of subtype-selective agents to avoid off-target effects while addressing drug-resistant epilepsy.

Here, we reported cryo-EM structures of heteromeric human M-channels in both *apo* and activator-bound states at high resolutions of 2.4–3.0 Å. Combined with functional assays, these structures revealed how XEN1101 and ICA-110381 engage distinct binding modes to stabilize activated 'up' VSDs. We further uncovered a stepwise gating mechanism in which PD-targeting modulators act cooperatively with PIP_2 binding at the VSD–PD interface to reinforce conformational transitions and promote pore opening. Together, these findings provide the structural basis of cooperative gating in heteromeric M-channels and establishe a mechanistic framework for subtype-specific modulation, with direct implications for the treatment of epilepsy and related channelopathies.

RESULTS

Structural and functional characterization of heteromeric M-channels

To reconstruct heteromeric M-channels, we first co-expressed codon-optimized full-length KCNQ2 (Uniprot O43526) and KCNQ3 (Uniprot O43525) with distinct C-terminal affinity tags. Whole-cell patch-clamp recordings in HEK293T cells confirmed that co-expression produced robust heteromeric currents, with amplitudes substantially larger than those generated by either subunit alone (Fig. 1a, b; Supplementary Table S1).

Using tandem affinity purification, we isolated channel complexes containing both KCNQ2 and KCNQ3 subunits. However, the low expression level initially limited cryo-EM particle collections. Guided by prior work on homomeric KCNQ structures, we truncated disordered regions at both termini to improve protein stability and yield[24-26] (Supplemen-

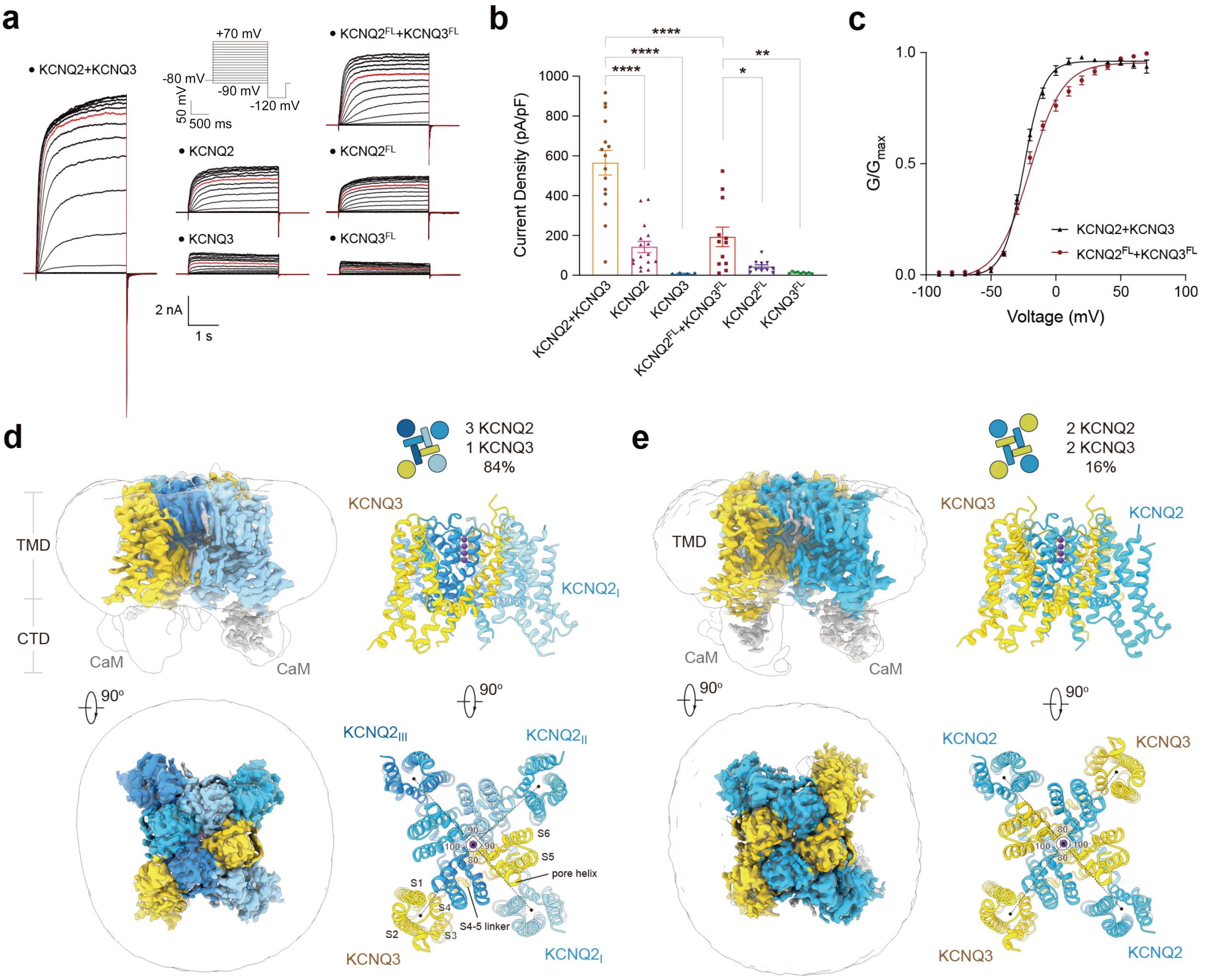

Fig. 1 Overall architecture of human M-channels with two distinct stoichiometries. a Representative whole-cell currents recorded from HEK293T cells expressing heteromeric KCNQ2/KCNQ3 channels, KCNQ2, or KCNQ3. Co-expression of KCNQ2 and KCNQ3 generated larger currents than either subunit expressed alone. Currents were elicited from −90 mV and stepped to +70 mV for 1,500 ms. Truncated constructs used for both structural and electrophysiological analyses are denoted as KCNQ2/3, whereas full-length constructs are referred to as $KCNQ2/3^{FL}$. **b** Quantification of current densities: 565.6 ± 61.66 pA/pF for KCNQ2+KCNQ3, 142.3 ± 28.30 pA/pF for KCNQ2, 9.44 ± 1.20 pA/pF for KCNQ3, 192.8 ± 48.89 pA/pF for $KCNQ2^{FL}$+$KCNQ3^{FL}$, 43.49 ± 9.15 pA/pF for $KCNQ2^{FL}$, and 13.14 ± 1.53 pA/pF for $KCNQ3^{FL}$ (n = 15, 16, 4, 12, 11, 9; mean ± SEM). One-way ANOVA was used for statistical analysis. $^{*}P < 0.05$; $^{**}P < 0.01$; $^{***}P < 0.001$; $^{****}P < 0.0001$. **c** Voltage-dependent activation of heteromeric KCNQ2/KCNQ3 channels. Truncated constructs (KCNQ2+KCNQ3, $V_{1/2} = -24.84 \pm 0.37$ mV, n = 15) exhibited activation properties comparable to full-length channels ($KCNQ2^{FL}$ + $KCNQ3^{FL}$, $V_{1/2} = -20.18 \pm 0.69$ mV, n = 10). Please refer to Materials and Methods for experimental details. **d**, **e** Cryo-EM structures of human M-channels resolved in two stoichiometries. The predominant assembly (84%) adopts an asymmetric 3:1 stoichiometry of KCNQ2 to KCNQ3 (**d**), while a minor population (16%) forms a staggered 2:2 stoichiometry (**e**). Shown here are side and extracellular views of cryo-EM density maps and corresponding atomic models, with KCNQ3 colored yellow and KCNQ2 blue. Within each stoichiometry, differences in the positioning of the VSDs relative to the PD between KCNQ2 and KCNQ3 are highlighted by distinct angles. For clarity, KCNQ2 subunits in the asymmetric assembly are labeled $KCNQ2_I$, $KCNQ2_{II}$, and $KCNQ2_{III}$, ordered counterclockwise from KCNQ3 in the extracellular view. All structural figures were prepared using ChimeraX[69].

tary Fig. S1). Notably, the C-terminal subunit interaction domain was retained in the engineered constructs[55,56]. These truncated constructs exhibited enhanced expression while preserving gating properties comparable to wild-type channels (Fig. 1a–c; Supplementary Table S1).

Following well-established protocols for protein purification, cryo-sample preparation, data acquisition, and processing, we obtained high-resolution three-dimensional reconstructions of heteromeric KCNQ2/KCNQ3 channels at 2.4–2.7 Å (Fig. 1d, e; Supplementary Figs. S2, S3a, b and Table S2). Although CaM was not co-expressed, densities corresponding to endogenous CaM were observed bound to the intracellular HA-HB hairpins, consistent with prior co-expression structures[17,21,26] (Fig. 1d, e; Supplementary Fig. S3b, c). Compared to the well-resolved transmembrane regions, the intracellular CaM-binding HA-HB hairpins and HC coiled-coil exhibited weaker densities, limiting accurate model building (Supplementary Fig. S3b). Therefore, subsequent analyses were focused primarily on the transmembrane regions.

At resolutions sufficient for reliable atomic modeling, the transmembrane region of the heteromeric KCNQ2/KCNQ3 complex adopts the canonical domain-swapped architecture of voltage-gated potassium channels. Individual subunits were distinguished by several structural hallmarks, including Tyr284 in KCNQ2 vs Thr323 in KCNQ3 near the extracellular vestibule, Tyr226 vs Cys255 within the S4–5 linker, and differences in extracellular loops (KCNQ2: residues 255–263, 9 amino acids (aa); KCNQ3: residues 284–302, 19 aa) (Supplementary Fig. S3d–h). These identifiers allowed unambiguous subunit assignment and revealed a dominant asymmetric assembly with a 3:1 stoichiometry of KCNQ2 to KCNQ3 (84%) and a minor staggered 2:2 complex (16%) (Fig. 1d, e; Supplementary Fig. S3i). The preferential enrichment of KCNQ2 likely reflects its higher expression level relative to KCNQ3 under the same conditions (Supplementary Fig. S3a, upper). Despite their differing compositions, the central PDs of the two assemblies are highly conserved, exhibiting similar radius profiles along the ion permeation path (Supplementary Fig. S3j, k).

To evaluate the physiological relevance of these stoichiometries, we generated concatemers with defined subunit arrangements corresponding to the observed assemblies (KCNQ2:KCNQ3 = 3:1 and staggered 2:2, designated KCNQ2/3/2/2 and KCNQ2/3/2/3, respectively), as well as the other two possible configurations (1:3 and neighboring 2:2, designated KCNQ2/3/3/3 and KCNQ2/3/3/2), followed by whole-cell patch-clamp recordings (Supplementary Fig. S4). The resulting macroscopic current densities and gating properties of KCNQ2/3/2/2, KCNQ2/3/2/3, and KCNQ2/3/3/2 closely recapitulate those of co-expressed KCNQ2/KCNQ3 channels (Supplementary Fig. S4). Notably, both KCNQ2/3/2/2 and KCNQ2/3/2/3 assemblies are structurally resolved in this study. For clarity, the three KCNQ2 subunits in the asymmetric 3:1 complex are designated KCNQ2$_{I}$, KCNQ2$_{II}$, and KCNQ2$_{III}$ in counterclockwise order from the unique KCNQ3 when viewed from the extracellular side. Hereafter, the heteromeric KCNQ2/KCNQ3 complexes are collectively referred to as the M-channels.

Structural differences between KCNQ2 and KCNQ3 subunits

To dissect the structural determinants underlying subunit heterogeneity, we sought to determine the cryo-EM structures of homomeric KCNQ2 and KCNQ3 channels using the same engineered constructs. While poor sample quality limited high-resolution reconstruction of KCNQ3, the structure of homomeric KCNQ2 was determined at 2.3 Å resolution (Supplementary Fig. S5 and Table S2). Structural comparison between the heteromeric M-channel and homomeric KCNQ2 revealed pronounced conformational changes associated with incorporation of the KCNQ3 subunit, most notably a counterclockwise rotation of the KCNQ3 VSD when viewed extracellularly (Fig. 2a). Similar subtype-dependent differences in VSD conformations were also observed across distinct stoichiometries of the heteromeric M-channels (Supplementary Fig. S3j).

The selectivity filter (SF) of the M-channel preserved the canonical TIGYG motif that coordinates a linear array of four K^+ ions, closely resembling that of homomeric KCNQ2[19,20,22]. However, sequence alignment across the KCNQ family revealed a notable divergence: KCNQ3 harbors a unique alanine immediately preceding the TIGYG motif, whereas other subtypes, including KCNQ2, contain a conserved threonine (Fig. 2b, c; Supplementary Fig. S1). Electrophysiological analysis confirmed this site as a key determinant of subtype-specific activity. The KCNQ3 A315T mutation produced robust currents comparable to those of KCNQ2, consistent with earlier reports[12,57,58]. By contrast, substitution of the corresponding threonine in KCNQ2 with alanine or isoleucine (T276A/I) may disrupt ion conduction or weaken subunit interactions, resulting in markedly reduced current amplitudes (Fig. 2c; Supplementary Fig. S6a). These effects recapitulate the loss-of-function phenotype of the pathogenic T276I variant associated with Ohtahara syndrome (early infantile developmental and epileptic encephalopathy, EIDEE)[59,60].

Within the VSD, additional differences were observed. The S4 helix of KCNQ3 adopts a more activated 'up' conformation, and an elongated loop spanning Arg227–Phe231 replaced the helical turn in KCNQ2 (Fig. 2d, e). Previous studies have suggested that the M-channel exhibits unique low-voltage activation, potentially arising from this pre-activated VSD of KCNQ3[61,62]. To test this, we designed a chimeric channel combining the PD of KCNQ2 with the VSD of KCNQ3. Expression of this chimera, either alone or co-expressed with wild-type KCNQ3, induced a pronounced hyperpolarizing shift in activation, with half-activation voltages ($V_{1/2}$) of −35.32 ± 1.71 mV and −33.85 ± 0.62 mV, respectively (Fig. 2f; Supplementary Fig. S6b). These results indicated that KCNQ3 contributes to heteromeric M-channel function primarily by tuning voltage dependence via its VSD, rather than forming a functional homomeric channel.

Together, these structural and functional analyses define how unique molecular features of KCNQ3 shape the function of heteromeric M-channels. Beyond intrinsic subunit composition, M-channel activity is further modulated by pharmacological modulators. We next examined two mechanistically distinct activators: the VSD-targeting ICA-110381 and the PD-targeting XEN1101 (Azetukalner), the latter currently in phase III clinical trials.

ICA-110381 selectively targets the KCNQ2 VSD

ICA-110381, a small-molecule M-channel activator with anticonvulsant properties, potentiated current amplitude and attenuated tail-current inactivation in a dose-dependent manner (Supplementary Fig. S7a, b). This effect was accompanied by an induced hyperpolarizing shift in voltage-dependent activation, with $V_{1/2}$ moving from −25.00 ± 0.56 mV to

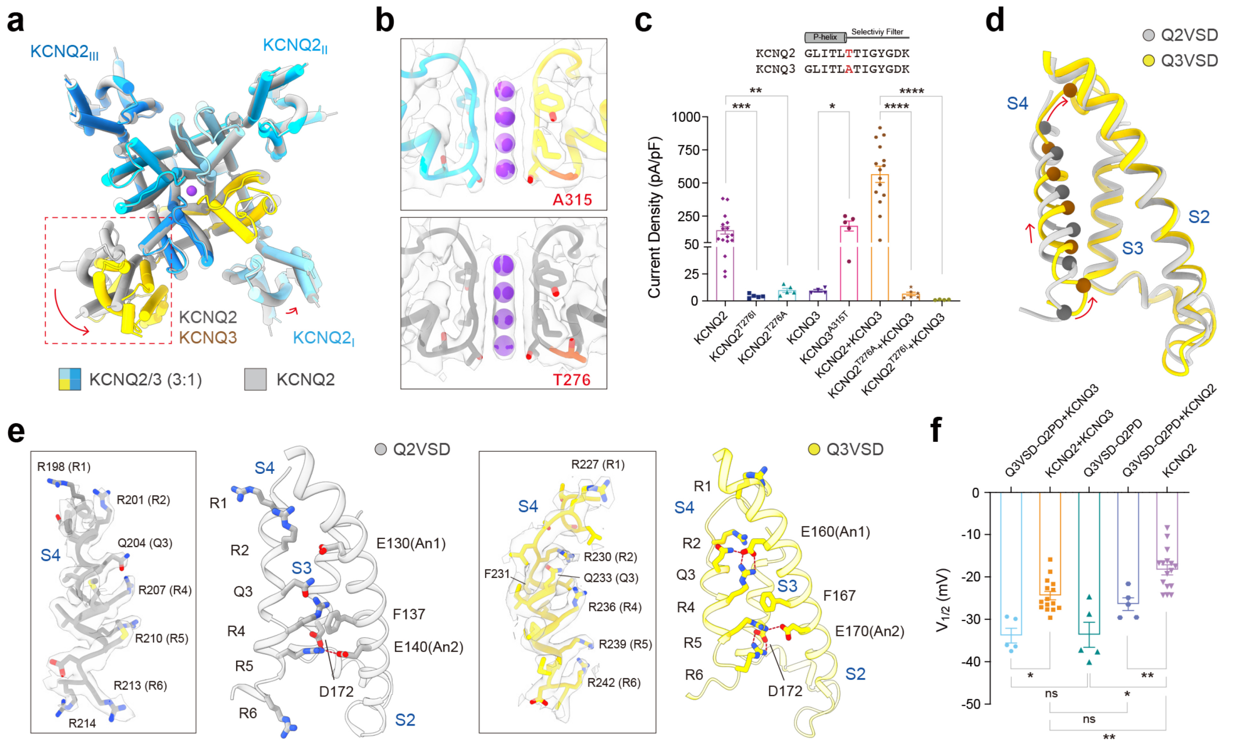

Fig. 2 **KCNQ3 confers low-voltage activation to human M-channels.** **a** Structural comparison of the transmembrane regions of the heteromeric M-channel (3:1 stoichiometry) and homotetrameric KCNQ2. The superimposed structures of the M-channel (domain colored) and KCNQ2 (gray) are aligned based on their central PDs, with transmembrane helices shown as cylinders. The KCNQ3 subunit exhibits a pronounced counterclockwise rotation of the entire VSD when viewed from the extracellular side. **b** Close-up view of the SF with superimposed EM densities, with bound K^+ ions indicated in purple. KCNQ3 harbors a unique Ala residue immediately preceding the SF, distinct from KCNQ2. **c** Functional analysis of the critical Ala residue in KCNQ3. Current densities are 4.39 ± 1.85 pA/pF for KCNQ2^{T276I}, 9.78 ± 1.93 pA/pF for KCNQ2^{T276A}, 175.41 ± 37.98 pA/pF for KCNQ3^{A315T}, 6.54 ± 1.59 pA/pF for KCNQ2^{T276A}+KCNQ3, and 1.06 ± 0.15 pA/pF for KCNQ2^{T276I}+KCNQ3 (n = 5, 5, 5, 6, 4; mean ± SEM). The sequence alignment shown above highlights the unique Ala position in KCNQ3. **d** Distinct VSD conformation in KCNQ3. Superimposed VSDs show that the S4 helix of KCNQ3 adopts an ‘up’ conformation compared to that of KCNQ2. **e** Structural comparison of VSDs in KCNQ2 and KCNQ3. Gating charge (GC) residues on S4 and conserved acidic/polar residues (An1, An2) on S2 are shown as sticks. Inset: EM density of the S4 helix in KCNQ3 reveals an elongated loop spanning Arg227–Phe231, in contrast to the canonical helical turn present in KCNQ2. **f** Electrophysiological characterization of the KCNQ3 VSD confirms its contribution to the low-threshold activation of M-channels. $V_{1/2}$ values are −33.85 ± 0.62 mV for Q3VSD-Q2PD+KCNQ3, −24.84 ± 0.37 mV for KCNQ2+KCNQ3, −35.32 ± 1.71 mV for Q3VSD-Q2PD alone, −26.48 ± 0.80 mV for Q3VSD-Q2PD+KCNQ2, and −18.78 ± 0.55 mV for KCNQ2 alone (n = 5, 15, 5, 5, 16; mean ± SEM). One-way ANOVA was used for statistical analysis (**c** and **f**). ns, no significance; $^{*}P < 0.05$; $^{**}P < 0.01$; $^{***}P < 0.001$; $^{****}P < 0.0001$.

−47.27 ± 1.87 mV (EC_{50} = 1.54 ± 0.18 μM), and a marked slowing of deactivation kinetics, as reflected by increased τ values (Fig. 3a; Supplementary Fig. S7a, b). Notably, ICA-110381 exhibited pronounced subtype selectivity: at 10 μM, it shifted KCNQ2 activation leftward by $\Delta V_{1/2}$ of −32.20 ± 2.19 mV, while KCNQ3 remained largely unaffected (Fig. 3b; Supplementary Fig. S7c, d).

To elucidate the structural basis underlying this selectivity, we determined cryo-EM structures of ICA-110381-bound M-channels in multiple conformational states and stoichiometric assemblies at resolutions ranging from 2.7 to 3.0 Å (Supplementary Fig. S8 and Table S2). Additional densities were immediately identified within the cavities of KCNQ2 VSDs, but not KCNQ3, providing direct structural evidence for subtype-specific engagement and the coexistence of both 3:1 and 2:2 heteromeric M-channel assemblies (Fig. 3c–e; Supplementary Fig. S9). Model building revealed ICA-110381 resided in a hydrophobic cavity of the KCNQ2 VSD, coordinated by Ile134 and Phe137 on S2, Phe168, Ile171, Asp172, Val175, and Leu176 on S3, and Leu206, Arg207, Ile209, and Arg210 on S4 across distinct conformational states and assemblies (Fig. 3f, left; Supplementary Fig. S9). Following our recently proposed nomenclature for drug-binding sites on voltage-gated ion channels, this site is designated site VC, referring to the **c**avity of **V**SD[19].

Sequence alignment identifies three binding residues unique to KCNQ2 that may contribute to ligand recognition, including Phe168 and Ile171 on S3 and Ile209 on S4. In KCNQ3, the corresponding residues are Leu198, Leu201, and Leu238, respectively. Particularly, Phe168 at site VC engages in π–π stacking with the aromatic ring of ICA-110381, a stabilizing feature absent in KCNQ3 due to leucine substitution. To evaluate their functional roles, we generated three single-point mutants, F168L, I171L, and I209L, and a combined triple mutant F168L/I171L/I209L. Electrophysiological analysis showed that both F168L and the triple mutant markedly reduced channel sensitivity to ICA-110381, whereas I171L and I209L had limited effects (Fig. 3f, right; Supplementary Fig. S7e). These results indicated Phe168 as the key determinant of subtype-selective recognition of ICA-110381 by KCNQ2.

Binding of ICA-110381 also triggered conformational rearrangements within KCNQ2 VSDs, while the PDs, including the S4–5 linker, remained largely unchanged across subunits compared to the *apo* structure. In a representative extracellular view, the VSD underwent a counterclockwise rotation, bringing S4 closer to the pore-forming S5 helix and strengthening interdomain contacts. Similar arrangements were observed across all KCNQ2 VSDs compared to the *apo* state, although the extent of rotation varied slightly in KCNQ2$_{I}$ and KCNQ2$_{II}$ across the different states of the 3:1 assembly (state-

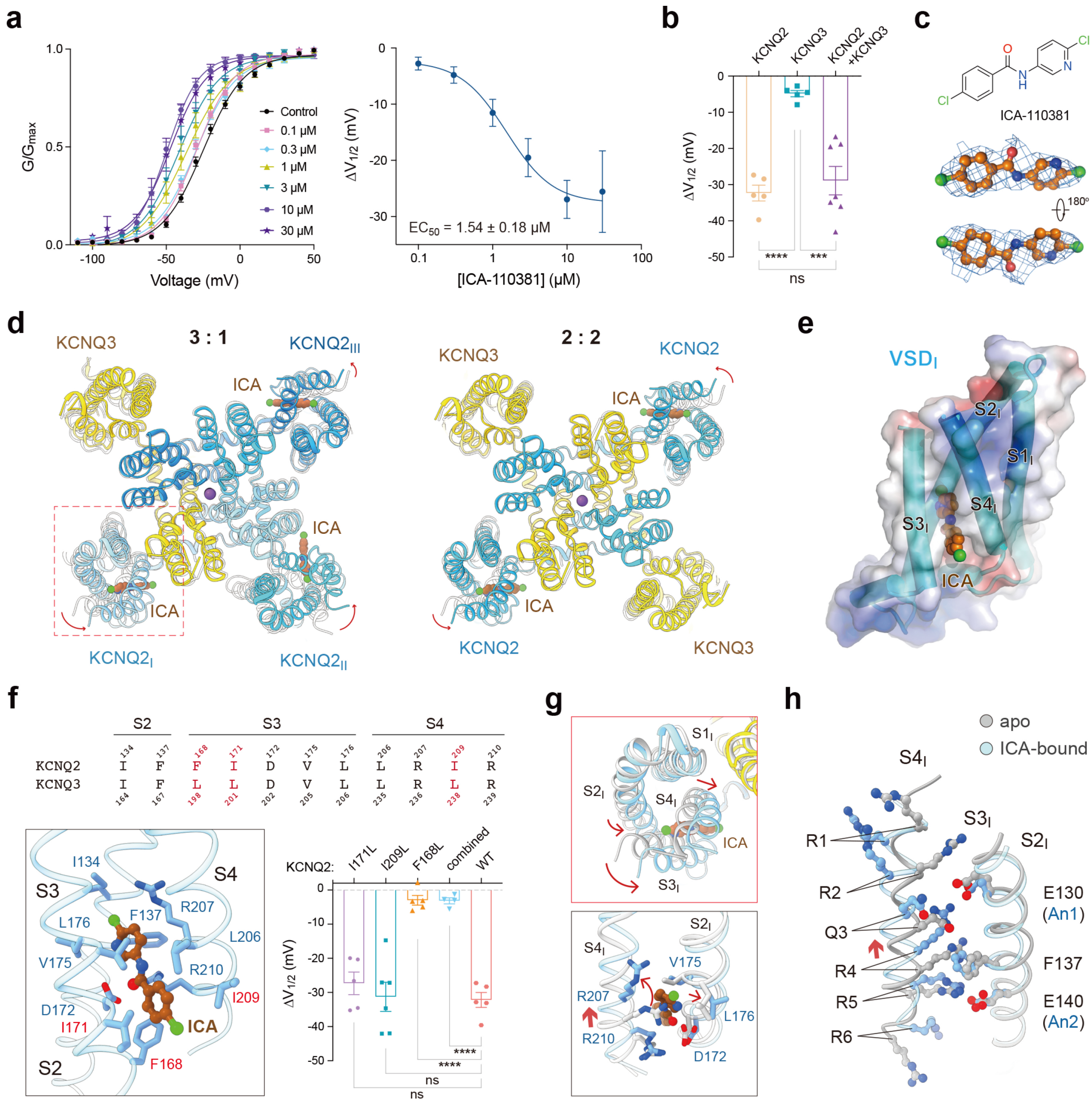

Fig. 3 ICA-110381 selectively activates M-channels via KCNQ2 VSDs. **a** Electrophysiological analysis of ICA-110381 effects on the M-channels. Left: Normalized activation curves recorded in the presence of increasing ICA-110381 concentrations. Right: Dose-dependent response of ICA-110381-induced activation shifts, with the EC_{50} value of 1.54 ± 0.18 µM. **b** Effects of 10 µM ICA-110381 on channel activation. $\Delta V_{1/2}$ values are −28.76 ± 3.92 mV for KCNQ2/3, −32.20 ± 2.19 mV for KCNQ2, and −4.71 ± 0.86 mV for KCNQ3 (n = 7, 5, 5; mean ± SEM). **c** Chemical structure and corresponding EM density of ICA-110381. **d** Selective binding of ICA-110381 to KCNQ2 VSDs. Shown here are the extracellular views of M-channels in complex with ICA-110381 at different stoichiometries. For the 3:1 stoichiometry, state-3, which exhibits the most pronounced conformational rearrangement, is selected for illustration. Superimposed *apo* (gray) and activator-bound (domain-colored) structures, aligned on their PDs, highlight local conformation changes, as indicated by red arrows. **e** Electrostatic surface of the KCNQ2 VSD with ICA-110381 bound, shown as ball-and-sticks. **f** Structural basis for subtype selectivity. Top: Structure-guided sequence alignment of binding residues, with KCNQ2- and KCNQ3-specific positions highlighted in red. Bottom left: Detailed coordination of ICA-110381 within the KCNQ2 VSD, with unique residues indicated in red. Bottom right: Functional validation of subtype selectivity. $\Delta V_{1/2}$ values at 10 µM ICA-110381 are −27.34 ± 3.30 mV for KCNQ2 I171L, −31.28 ± 4.28 mV for KCNQ2 I209L, −3.01 ± 1.41 mV for KCNQ2 F168L, and −3.15 ± 0.89 mV for the combined mutant (n = 5, 6, 5, 4; mean ± SEM). **g** Conformational rearrangements of the KCNQ2 VSD upon ICA-110381 binding. Shown here are the superimposed *apo* (gray) and ICA-110381-bound (light blue) structures, with the local shifts indicated by red arrows. **h** ICA-110381 stabilizes an 'up' VSD. GC residues on S4 and conserved acidic/polar residues (An1, An2) on S2 are shown as sticks, with displacement directions highlighted by red arrows. One-way ANOVA was used for statistical analysis (**b** and **f**). ns, no significance; $^*P < 0.05$; $^{**}P < 0.01$; $^{***}P < 0.001$; $^{****}P < 0.0001$.

1/2/3) (Fig. 3g, upper; Supplementary Fig. S8f). Concurrently, ICA-110381 stabilized S4 in an 'up' conformation relative to the *apo* state (Fig. 3g, lower, and 3h). This stabilization mirrors the mechanism proposed for ztz240, in which ligand binding traps the VSD in an activated state, strengthens VSD-PD coupling, and promotes channel opening[22,24]. Together, these results demonstrate that ICA-110381 activates M-channels by selectively stabilizing the activated KCNQ2 VSDs, conferring subunit-specific modulation within heteromeric assemblies.

XEN1101 engages all four fenestrations of the PD

XEN1101 (Azetukalner) is a next-generation small-molecule opener of neuronal KCNQ channels, currently in late-stage clinical development for focal epilepsy and other seizure disorders[50-52]. As a derivative of retigabine, the first FDA-approved KCNQ channel modulator, XEN1101 was rationally designed to circumvent the metabolic instability and adverse effects of its predecessor[63]. Functionally, XEN1101 induced a significant hyperpolarizing shift in channel activation, moving the $V_{1/2}$ from −22.83 ± 0.58 mV to −67.61 ± 4.44 mV, with an EC_{50} of 0.66 ± 0.13 µM (Fig. 4a; Supplementary Fig. S10).

Following the same strategy applied to the *apo* and ICA-110381-bound complexes, we determined the high-resolution cryo-EM structures of the M-channel in complex with XEN1101 (Supplementary Fig. S11). The densities were well-resolved, enabling unambiguous modelling of both the channel and the bound ligands (Fig. 4b; Supplementary Figs. S12, S13, and Table S2). Similar to retigabine, XEN1101 occupied all four fenestrations of the PD through a conserved binding pose across different conformational states and stoichiometric assemblies, regardless of the specific KCNQ subunit composition[21,22] (Supplementary Fig. S13). Each pocket was enclosed by the S5 and S6 helices of adjacent subunits and the S4–5 linker of one contributing subunit (Fig. 4c, d).

Detailed inspection of heteromeric KCNQ2–KCNQ3 interfaces revealed a highly conserved binding pattern. At the interface between $KCNQ2_{III}$ and KCNQ3, the pocket was composed of residues Leu299, Ile300, Ser303, and Phe304 on S6 of $KCNQ2_{III}$, together with Leu250 and Ile254 on the S4–5 linker of KCNQ3, Trp265, Phe269, and Leu272 on its S5 helix, and Phe344, Pro347, and Leu351 on its S6 helix (Fig. 4e, upper left). This predominantly hydrophobic cavity was well-suited for ligand accommodation. Within this pocket, the amide group of XEN1101 engaged in two stabilizing hydrogen bonds — one with the backbone carbonyl of Leu299 in $KCNQ2_{III}$ and another with the indole nitrogen of Trp265 in KCNQ3. In addition, the aromatic core of XEN1101 formed π–π stacking with Trp265 of KCNQ3, further stabilizing ligand binding. A similar binding pattern was observed at the second heteromeric interface between KCNQ3 and $KCNQ2_{I}$ and the two homomeric KCNQ2–KCNQ2 interfaces, with only one difference: Ile254 in KCNQ3 was replaced by Val225 in KCNQ2, slightly altering the hydrophobic contact with the 3,3-dimethylbutanoyl tail of XEN1101 but leaving overall binding largely unaffected (Fig. 4e). This conservation across interfaces explained the nearly equivalent occupancy of XEN1101 at all four PD fenestrations.

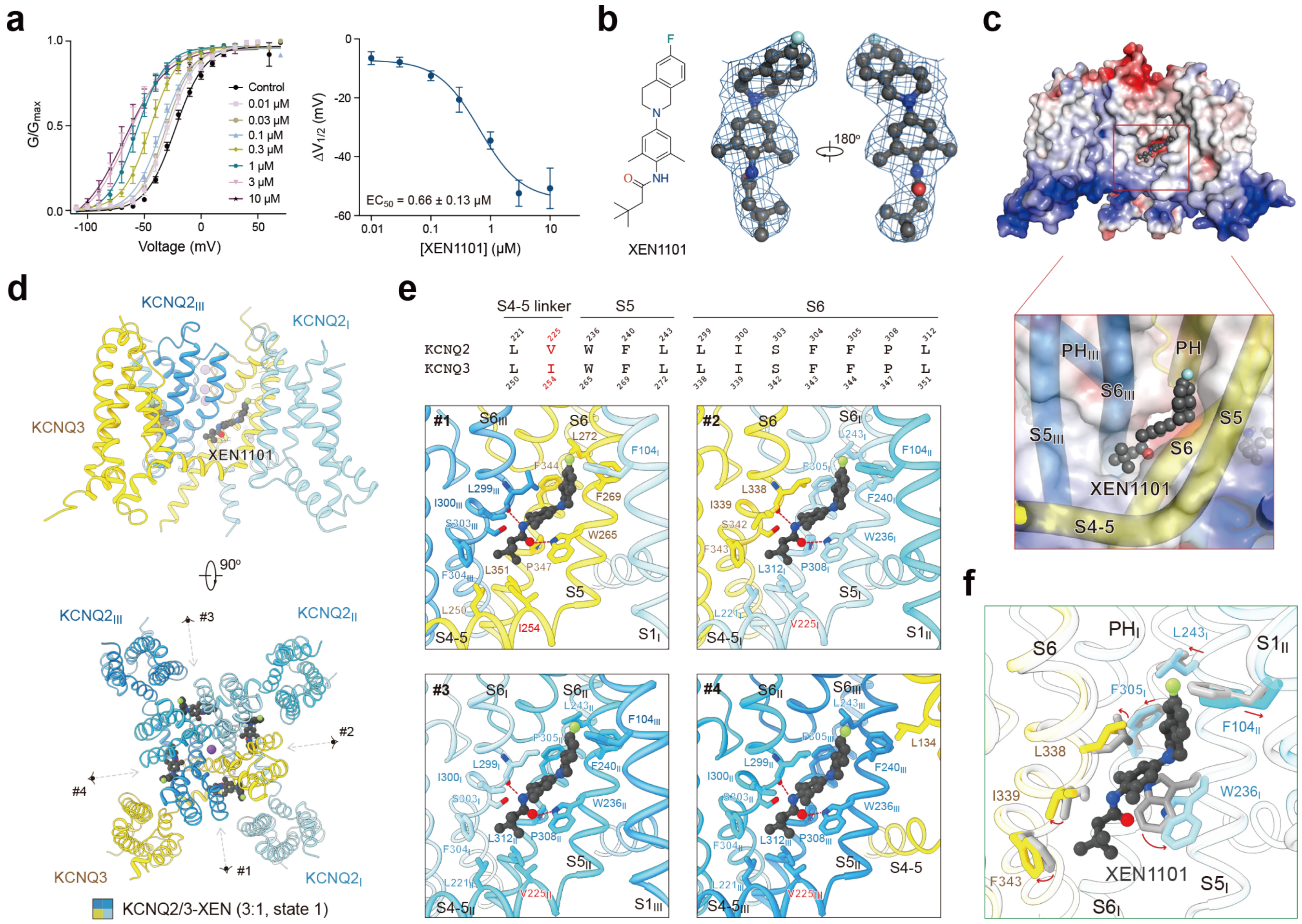

Fig. 4 PD-targeting activation of the M-channel by XEN1101. **a** Electrophysiological analysis of XEN1101 effects on heteromeric M-channels. Left: Normalized voltage-dependent activation curves recorded at increasing XEN1101 concentrations. Right: Dose-dependent response of XEN1101-induced activation shifts, with the EC_{50} value of 0.66 ± 0.13 µM. **b** Chemical structure and corresponding EM density of XEN1101. **c** Electrostatic surface of the M-channel transmembrane region in complex with XEN1101. Inset: XEN1101 binds to the fenestration formed by the adjacent PDs from neighboring subunits. **d** Binding of four XEN1101 molecules to distinct fenestrations. For the 3:1 stoichiometry, state-1, which most closely resembles the *apo* structure, was selected for illustration. Shown here are the side and extracellular views of the XEN1101-bound M-channel. Two molecules of XEN1101 bind at heterotypic KCNQ2–KCNQ3 interfaces (sites #1 and #2), while the remaining two occupy homotypic KCNQ2–KCNQ2 interfaces (sites #3 and #4). **e** Conservation of the XEN1101-binding pocket between KCNQ2 and KCNQ3. Top: Structure-guided sequence alignment of binding residues, with subtype-specific positions highlighted in red. Bottom: Detailed coordination of XEN1101 at each fenestration site, with unique residues indicated by red. **f** Local conformation rearrangements induced by XEN1101. Shown here are superimposed *apo* (gray) and XEN1101-bound (domain-colored) structures, with ligand binding-induced structural shifts indicated by red arrows.

Ligand binding was also accompanied by local conformational adjustments, most notably in the indole-bearing tryptophan residues. Trp236 in KCNQ2, or the corresponding Trp265 in KCNQ3, underwent a pronounced rotation to enable π–π stacking with XEN1101. A subtle outward displacement of the neighboring S6 helix further expanded the pocket, optimizing ligand accommodation (Fig. 4f). Collectively, these structural adaptations highlighted a conserved PD-binding mode of XEN1101 on heteromeric M-channels.

Cooperative gating induced by PD-targeting modulators

Beyond retigabine, the mechanisms of action for several PD-targeting KCNQ activators, including cannabidiol (CBD), HN37, Ebio1, and QO-83 (PDB: 8XO1), have been elucidated in homomeric channels[24,25]. In addition to these exogenous agents, endogenous cofactors are essential for channel activation, particularly CaM and PIP_2. PIP_2 binding is critical for channel opening, and its depletion by phospholipase C rapidly suppresses M currents[62]. Although we did not capture the M-channel in an open state simultaneously bound to XEN1101 and PIP_2, a distinctive cooperative gating mode conferred by heteromeric assemblies was observed. It provides unique insights into their synergistic activation, a feature not observed in homomeric KCNQ channels[17,20-22,27].

Despite the conserved occupancy of all four fenestrations by XEN1101, multiple XEN1101-bound states were resolved at high resolutions of 2.5–2.8 Å (Supplementary Figs. S11, S12, and Table S2). Notably, all structures retained the predominant asymmetric 3:1 and the minor staggered 2:2 stoichiometry of KCNQ2 to KCNQ3 (Supplementary Fig. S12b), as confirmed by the abovementioned signature residues and subtype-specific features of the S4 helices. The conformational changes induced by XEN1101 binding were observed primarily within the KCNQ2 VSDs, rather than reflecting altered channel composition (Fig. 5a).

Viewed from the extracellular side, the three KCNQ2 VSDs rotated sequentially in a counterclockwise order: $KCNQ2_I$ rotated first, followed by the adjacent $KCNQ2_{II}$ and then $KCNQ2_{III}$. Only the reconstruction in which all KCNQ2 VSDs adopted rotated conformations was obtained at lower resolution, owing to the limited number of particles (Supplementary Figs. S11, S12, and Table S2). These intermediate states, designated states 1–4, likely represent progressive stages of VSD transition (Fig. 5a; Supplementary Video S1). Despite their closed PDs, the VSD rearrangements closely resembled those observed in homomeric KCNQ2 bound to HN37 and PIP_2, in which the pore is open[24] (Fig. 5a, right). These observations suggest that the heteromeric M-channel activates through a stepwise, cooperative process.

Closer inspection of the PD–VSD interfaces revealed that ligand occupancy critically modulates coupling. In *apo* M-channels, two unidentified sterol-like densities were consistently observed at the interface between the KCNQ2 VSD and pore, but were absent from the KCNQ3 VSD–PD interface. These densities, designated ligand-a (intracellular side) and ligand-b (extracellular side), appeared to tether the VSD to the PD (Fig. 5b). Upon XEN1101 binding, ligand-b densities were displaced by steric exclusion, with the site occupied by XEN1101 and nearby residues including $Trp288_{III}$, $Ile115_I$, and $Glu117_I$ (Fig. 5c). As VSD rotation progressed, the density of ligand-a disappeared, and S4 adopted an activated ‘up’ conformation similar to that of KCNQ3, with S1 moving outward from the PD (Fig. 5b, d). This reorganization created a lipid-accessible cavity formed by S1, S4, and S6 of one subunit and S5 and the S4–5 linker of the neighbor, providing an ideal pocket for PIP_2 accommodation (Fig. 5b). In the open KCNQ2 structure, PIP_2 stabilized this interface through hydrogen bonds with Arg87 on S1, Arg214 on S4, Lys327 on S6, and Lys230 on S5 of the adjacent subunit, reinforcing VSD-PD coupling and promoting outward movement of the S6 helices to open the pore (Fig. 5e)[24].

Together, these structural snapshots suggested a cooperative mechanism for M-channel activation. Binding of exogenous PD-targeting activators perturbed lipid interactions at the VSD–PD interface, initiating sequential VSD rotations and creating a permissive pocket for PIP_2 engagement. PIP_2 then reinforced VSD-PD coupling and drove splaying of the S6 helices, culminating in pore opening. In contrast to the synchronous transitions of homomeric channels, heteromeric M-channels underwent sequential conformational changes across KCNQ2 subunits, providing mechanistic insights into cooperative gating (Fig. 5f). While the precise temporal order of PIP_2 engagement remained unresolved, the present structures provided critical intermediates and mechanistic evidence for cooperative opening in heteromeric M-channels.

DISCUSSION

This study aimed to address the central question in the KCNQ field: how the molecular architecture of heteromeric M-channels underlies their physiological dominance and therapeutic relevance. High-resolution cryo-EM structures of KCNQ2/KCNQ3 assemblies, combined with functional analyses, reveal a predominant asymmetric 3:1 stoichiometry of KCNQ2 to KCNQ3, alongside a minor but stable staggered 2:2 population. Strikingly, this compositional heterogeneity (78–84% 3:1 across conditions) is consistently observed in *apo* and modulator-bound datasets, and the selective engagement of KCNQ2-targeting modulator ICA-110381 directly validates both assemblies. Although additional stoichiometries corresponding to neighboring 2:2 or 1:3 KCNQ2:KCNQ3 assemblies were not structurally captured under our experimental conditions, electrophysiological analyses of engineered concatemers showed that channels representing all four possible assemblies generated larger currents than KCNQ2 homomers. Notably, the 1:3 concatemer induced a pronounced negative shift in the voltage-dependent activation. Collectively, these results provide compelling evidence for the coexistence of heteromeric channels with distinct subunit stoichiometries under physiological conditions, uncovering an additional layer of structural and functional heterogeneity.

Our findings further delineate subunit-specific contributions to M-channel function. KCNQ3 uniquely harbors an alanine preceding the selectivity filter that alters conductance in homomeric channels, while its pre-activated voltage sensors lower the activation threshold of heteromers. KCNQ2, by contrast, provides a unique pharmacological scaffold, with ICA-110381 engaging exclusively hydrophobic pockets in KCNQ2 VSDs. Co-expression of KCNQ2 and KCNQ3 yielded robust currents larger than either homomer alone, indicating the physiological necessity of heteromeric assembly. This division of labor between KCNQ2 and KCNQ3 explains why heteromeric M-channels outperform homomers in regulating neuronal excitability and highlights the emergent properties arising from heteromerization.

The structures also provide a mechanistic interpretation of

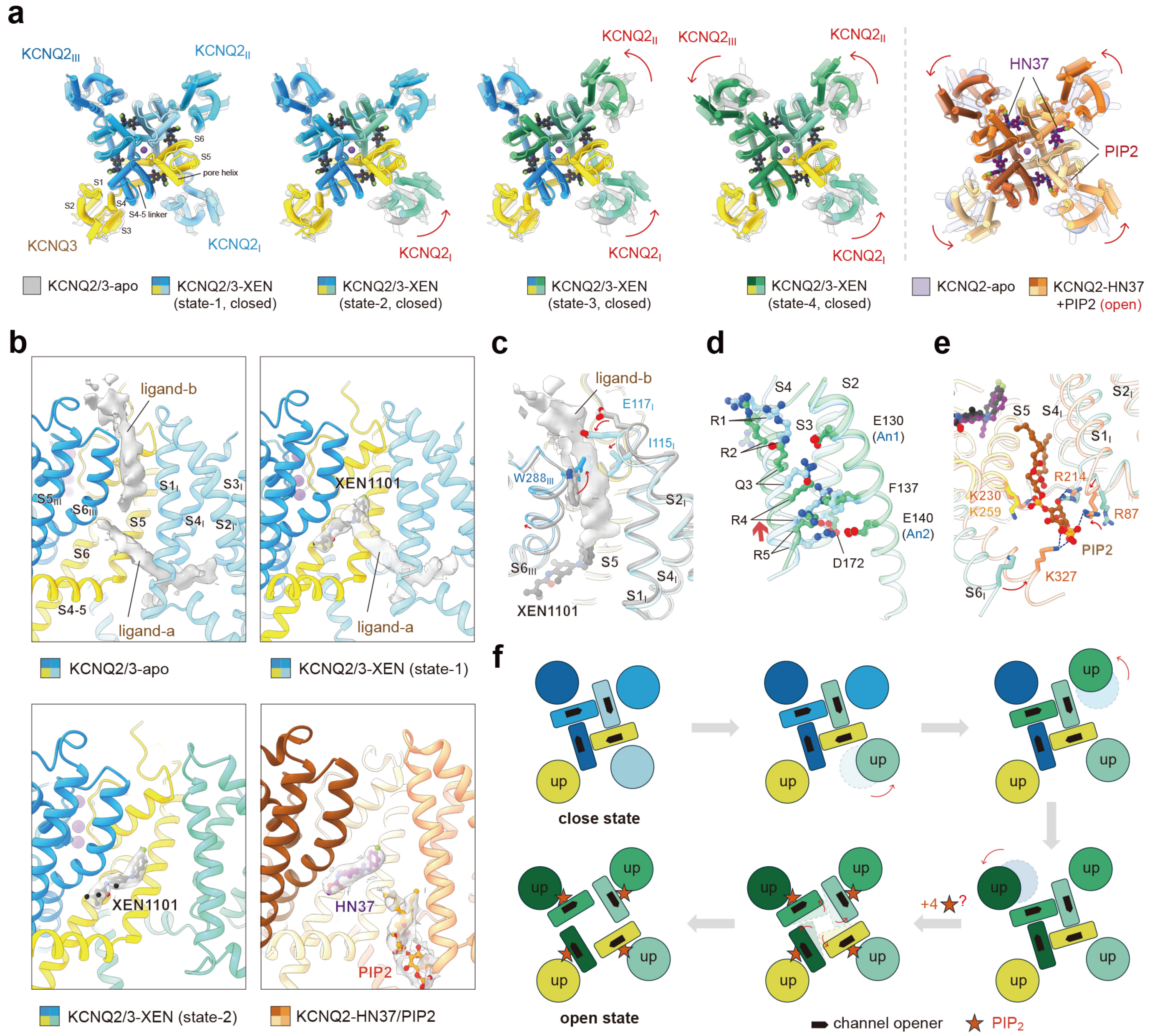

Fig. 5 Cooperative gating of human M-channels by pore-targeting modulators and PIP$_2$. a KCNQ2 VSDs adopt multiple conformations in the presence of XEN1101. Four distinct states were resolved from a single dataset: state-1 with three 'down' KCNQ2 VSDs, state-2 with one 'up' KCNQ2 VSD, state-3 with two 'up' KCNQ2 VSDs, and state-4 with all 'up' VSDs. Shown here are superimposed structures of each state (domain-colored) aligned with the *apo* channel (gray) by their PDs. For comparison, the open KCNQ2 structure bound to another pore-targeting opener, HN37, along with PIP$_2$, is shown on the right, with similar VSD displacements indicated by red arrows. **b** Ligand occupancy at the PD–VSD interface across states. In the *apo* channel, the KCNQ2 VSD–PD interface engages two unidentified ligands, designated ligand-a on the intracellular side and ligand-b on the extracellular side. Upon XEN1101 binding, only ligand-a remains at interfaces containing 'down' VSDs, while PDs adjacent to 'up' VSDs are engaged solely by XEN1101. In the presence of both HN37 and PIP$_2$, the PD–VSD interface is additionally occupied by a well-resolved PIP$_2$ density. **c**–**e** Structural transitions between states. Binding of XEN1101 introduces steric clashes with the ligand-b density (**c**). VSD rearrangements accompanying the 'down-to-up' transition mimic those observed in KCNQ3, as described in Fig. 2 (**d**). PIP$_2$ binding reinforces coupling between the VSD and S6 helix, thereby promoting channel opening (**e**). **f** Schematic representation of cooperative gating in human M-channels. Sequential counterclockwise rotation of adjacent KCNQ2 VSDs, viewed from the extracellular side, progressively creates space for PIP$_2$ binding, which, together with pore-targeting activators, drives channel opening.

disease mutations. Mapping pathogenic variants onto heteromeric M-channels revealed a striking convergence of DEE- and BFNS-associated mutations at residues within the P-loop and voltage sensors, particularly the signature SF motif and gating-charge residues essential for ion permeation and gating transitions (Supplementary Fig. S14 and Table S3). Perturbations at these sites likely destabilize pore architecture or impair voltage sensing, leading to reduced M-current and neuronal hyperexcitability. Mutations within the VSD–PD interface, including those directly involved in PIP$_2$ recruitment such as R214W in KCNQ2, may instead abolish PIP$_2$-mediated coupling (Supplementary Fig. S14). These observations not only clarify how diverse mutations converge on common structural hotspots but also suggest opportunities for genotype-tailored therapies, in which modulators could be selected to compensate for specific structural defects.

Our results also expand the pharmacological landscape of M-channel modulation. ICA-110381 engages a unique hydrophobic pocket within KCNQ2 VSDs, stabilizing the activated conformation and establishing a paradigm for subtype-selective modulation. By contrast, XEN1101 exploits a cooperative gating mechanism, progressing through multiple conformational intermediates. Binding of XEN1101 within PD fenestrations displaces sterol-like lipids, triggers sequential VSD rotations, and reorganizes the PD–VSD interface to favor PIP_2 recruitment. PIP_2, in turn, reinforces interdomain coupling through conserved basic residues, driving outward splaying of the S6 helices and promoting pore opening. Given that CaM was not additionally co-transfected during expression, we assessed whether endogenous CaM is sufficient for this cooperative gating mechanism. Cryo-EM analysis of samples co-expressing KCNQ2, KCNQ3 and CaM under XEN1101 treatment revealed the same heteromeric assemblies, similar intermediate states, and comparable state distributions as those observed without CaM co-expression (Supplementary Fig. S15 and Table S4), indicating that the stepwise gating behavior is intrinsic to heteromeric M-channels.

The identification of distinct stoichiometries and conformational states of heteromeric M-channels is primarily based on heterogeneous analysis of high-resolution structural features derived from reconstructed classes of purified overexpressed samples. This approach may be limited by the sensitivity of current algorithms in detecting low-abundance particles representing alternative stoichiometries or conformational states. Therefore, new approaches are needed to investigate the endogenous assembly of M-channels and to validate their native assembly states under physiological conditions. Concurrently, the stepwise conformational changes described in this study have thus far been observed only in the 3:1 KCNQ2:KCNQ3 assembly; therefore, it would be valuable in future studies to determine whether similar mechanisms also occur in other low-abundance assemblies using structural and complementary biophysical approaches.

In summary, our study establishes the structural basis of heteromeric M-channel assembly, cooperative gating, and pharmacological modulation. By integrating stoichiometric heterogeneity, subunit-specific contributions, and disease-mutation mapping, we provide a mechanistic framework bridging molecular architecture to neuronal excitability and epilepsy. Beyond fundamental insights, the structural elucidation of KCNQ2-specific sites lays the groundwork for rational design of subunit-selective modulators, paving the way for precision therapies for KCNQ-related channelopathies.

MATERIALS AND METHODS

Cell culture and transient expression of human KCNQ subunits in HEK293F cells

HEK293F suspension cells (gift of Sino Biological Inc.) were maintained in SMM 293T-II medium (Sino Biological Inc.) at 37 °C under 5% CO_2 and 60% humidity.

Codon-optimized cDNAs encoding full-length human KCNQ2 (Uniprot O43526) and KCNQ3 (Uniprot O43525) were synthesized (BGI Geneland Scientific, Shenzhen) and cloned into the pCAG vector separately with a FLAG-tag and Twin-Strep-tag at the C-terminus, respectively. To enhance expression, distal N- and C-terminal regions of both KCNQ2 and KCNQ3 were truncated, yielding $KCNQ2^{EM}$ (Ala62–Ser672) and $KCNQ3^{EM}$ (Ala89–Ser665), each comprising the S0–S6 transmembrane segments with flanking intracellular helices[25]. Notably, the C-terminal subunit interaction domain was fully retained to preserve heteromeric assembly of the KCNQ2/KCNQ3 complex[55,56]. All plasmids intended for transient expression were verified through DNA sequencing.

Cells were transfected at a density of 1.5–2.0 × 10^6 cells per mL. For each one-liter cell culture, a mixture of 1.5 mg expression plasmids of heteromeric KCNQ, including 0.75 mg each of KCNQ2 and KCNQ3, were pre-incubated with 3 mg 40-kDa linear polyethylenimines (Hieff Trans® PEI MW40000, YEASEN) in 50 mL fresh medium for 15–30 min before adding to the culture. Recombinant co-expression of KCNQ2/3 complexes was achieved under these conditions.

Protein purification of human KCNQ2/KCNQ3 complexes

At approximately 48 h after transfection, 12 L of transfected HEK293F cells were harvested by centrifugation at 3,600× *g* for 10 min and resuspended in the lysis buffer containing 25 mM HEPES (pH 7.4), 150 mM KCl, protease inhibitor cocktails (SelleckChem), and 1 mM phenylmethanesulfonyl fluoride (PMSF, Sigma-Aldrich). The suspension was homogenized and then supplemented with n-dodecyl-β-D-maltopyranoside (DDM, Anatrace) to a final concentration of 1% (w/v) and cholesteryl hemisuccinate Tris salt (CHS, Anatrace) to 0.1% (w/v). After incubation at 4 °C for 2 h, the mixture was centrifuged at 32,000× *g* for 45 min, and the supernatant was applied to the anti-Flag M2 affinity gel (Sigma-Aldrich) for affinity purification. The resin was rinsed twice with 5 column volume (CV) buffer A, which contains 25 mM HEPES (pH 7.4), 150 mM KCl, 0.06% (w/v) DDM, and 0.006% (w/v) CHS, as well as protease inhibitor cocktails, and rinsed three times with 2 CV buffer B, which contains a different detergent by 0.06% (w/v) GDN. Target proteins were eluted with 6 CV buffer B supplemented with 0.4 mg/mL FLAG peptide. The eluent was then applied to Strep-Tactin Sepharose (IBA) and allowed to flow through by gravity. The target proteins were eluted with buffer B supplemented with 2.5 mM desthiobiotin (IBA). The eluent was then concentrated using 100-kDa molecular weight cut-off Amicon filter units (Millipore) and subjected to size-exclusion chromatography (Superose 6 Increase 10/300 GL column, GE Healthcare) pre-equilibrated with running buffer containing 25 mM HEPES (pH 7.4), 150 mM KCl, and 0.02% GDN. Peak fractions were pooled and concentrated to 4–6 mg mL^{-1}.

For preparation of ligand-bound complexes, XEN1101 and ICA-110381 stocks in DMSO (MCE) were diluted with gel filtration buffer and mixed with purified protein at a final concentration of 1 mM, with the concentration of DMSO below 1% (v/v). All the mixtures were incubated at 4 °C for 30 min before cryo-grid preparation.

Cryo-EM sample preparation and data acquisition

Ni-Ti grids (M01-Au300-R1.2/1.3, Nano Dimension Ltd.) were glow-discharged before use. Freshly purified M-channel complexes, with or without ligands, were applied to grids in a Vitrobot Mark IV chamber operated at 8 °C and 100% humidity. After blotting for 3.5 s, grids were plunge-frozen into liquid ethane and cooled by liquid nitrogen.

Data were collected on a 300 kV Titan Krios G4 cryogenic electron microscope (Thermo Fisher Scientific), equipped with a Gatan K3 direct electron detector and a GIF Quantum energy filter. Micrographs were captured using Falcon IVi (Thermo Fisher Scientific) in EC mode at a nominal magnification of 130,000×, corresponding to a calibrated pixel size of 0.936 Å. Data were acquired at a preset defocus range of −1.2 µm to −1.6 µm. Each EER-format movie stack was exposed within a 0.79-µm spot size and accumulated a total electron dose of approximately 50 $e^-/Å^2$ in EPU (Thermo Fisher Scientific). Subsequently, the movie stacks underwent alignment, summation, and dose-weighting using cryoSPARC live[64].

Cryo-EM data processing

A total of 5,578/6,443/5,745/6,852 cryo-EM micrographs were collected for KCNQ2/KCNQ3-*apo*/ICA-110381/XEN1101 and KCNQ2 homomer, respectively. During cryoSPARC live preprocessing, patched CTF estimation was implemented.

For the KCNQ2/KCNQ3-*apo* dataset: 787,548 particles were picked using a pre-trained general Topaz model[65], and subsequent 2D classification was performed with extracted bin-2 particles. Particles from good 2D Class averages with clear secondary structure features are used for *ab initio* reconstruction. The resulting 280,040 particles from the best 3D reconstruction were selected for another round of 2D Classification. The best particles after 2D classification were used to train a new Topaz model, which re-picked 1,560,372 particles from the collected micrographs. The new set of bin-2 particles underwent multiple rounds of 2D classification and continuous heterogeneous refinement. Subsequently, 1,184,540 particles were re-extracted into bin-1 and underwent three additional rounds of heterogeneous refinement, yielding a 2.4 Å NU-refinement reconstruction in a mixed conformation. To resolve the conformational heterogeneity, we conducted 3D variability analysis and reference-free 3D classification on the selected 789,952 particles. The resulting representative classes were used as references for further heterogeneous refinement, followed by NU-local refinement. This workflow successfully separated the particles into distinct classes corresponding to different VSD conformations (Supplementary Fig. S2).

For the KCNQ2 dataset: 1,674,039 bin-2 particles were selected after particle picking and 2D classification. Heterogeneous refinement was performed using one good reference (imported from EMD-30443) and two junk decoy references (generated from *ab-initio* reconstruction jobs). After the first round of 3D classification, particles from the two junk classes underwent another round of 2D classification and selection, then were merged with the particles from the good 3D class. Subsequently, 1,330,171 bin-1 particles were extracted and subjected to heterogeneous refinement to select the best class. NU-local refinement from 928,950 particles was then performed to yield a 2.3 Å reconstruction with C4 symmetry (Supplementary Fig. S5).

For the KCNQ2/KCNQ3-ICA-110381 dataset: 1,085,120 bin-2 particles were selected after particle picking and 2D classification. Heterogeneous refinement was performed using one good reference (*apo* state KCNQ2/3 3:1) and two junk decoy references (generated from *ab-initio* reconstruction jobs). Particles from the best class (848,024 particles) were selected and underwent another round of 2D classification for cleaning. Subsequently, 828,566 bin-1 particles were extracted to perform heterogeneous refinement. The best class, containing 526,850 particles, yielded a 2.6 Å reconstruction but displayed heterogeneity in the VSDs. Reference-free 3D classification was used to classify potential movements in the VSD domains. Different parameters were tested, including class number (4 to 6), filter resolution (4 Å to 6 Å), and class similarity (0 to 0.5). The combination of 4 classes, a filter resolution of 6 Å, and a class similarity of 0 provided good classification of different assemblies and states. These four classes were then selected as references for heterogeneous refinement. Finally, each class was selected and refined independently to yield the final reconstructions (Supplementary Fig. S8).

For the KCNQ2/KCNQ3-XEN1101 dataset: 1,423,284 bin-2 particles were selected after particle picking and 2D classification. A subset of 489,938 particles was used to perform *ab-initio* reconstruction into 3 classes. The output class from *ab-initio* reconstruction with correct 3D features of a tetrameric channel was used as a reference in the subsequent heterogeneous refinement, along with two junk decoy references. From this, 1,129,752 particles were selected, re-extracted at bin-1, and refined to 2.3 Å resolution, although heterogeneous VSD features were observed. The dataset was further cleaned by heterogeneous refinement to obtain a pool of 788,022 'clean' particles for heterogeneity analysis. 3DVA and 3D classification were performed in parallel to distinguish potential distinct 3D conformations and assemblies of the heteromeric channel. Five distinct classes representing different states or assemblies were selected as references, together with a junk decoy map, to classify all 788,022 particles. Each distinct representative class was then selected and refined independently after heterogeneous refinement to achieve high-resolution reconstructions (Supplementary Fig. S11).

The KCNQ2/KCNQ3-CaM-XEN1101 dataset was processed similarly to the KCNQ2/KCNQ3-XEN1101 dataset. A total of 1,023,557 particles were extracted from 5,663 micrographs to perform 2D classification cleaning and heterogeneous refinement using the same three references. The 692,571 cleaned particles, which could be reconstructed at 2.6 Å, were subjected to heterogeneity analysis and assigned into five distinct classes. Individual NU-refinement was then performed for each class to yield the final reconstruction.

Model building and refinement

The initial models for KCNQ in different complexes were adapted from the *apo* state homotetrameric KCNQ2 structure (PDB: 7CR3) and subjected to manual inspection and adjustments in COOT[66]. CIF restraint files for the two ligands (XEN1101 and ICA110381) were generated from their SMILES strings using the grade2 server (https://grade.globalphasing.org/cgi-bin/grade2_server.cgi). The ligands were then manually built and refined in Coot, docked into the target protein, and further refined based on the corresponding density. Refinement against the corresponding map was carried out using the Real-space Refinement option in PHENIX[67]. Further structure optimization was performed with ISOLDE[68], followed by a final round of Real-space Refinement in PHENIX[67]. Detailed validation results for the model refinement are provided in Supplementary Table S2.

Whole-cell electrophysiology

HEK293T cells were plated onto glass coverslips and transiently co-transfected with 1 μg expression plasmid (0.5 μg each plasmid of KCNQ2 and KCNQ3 for co-transfection) and 0.1 μg eGFP, using Lipofectamine 3000 (Invitrogen). Whole-cell patch-clamp recording for GFP-positive cells was performed at room temperature after 18 h of transfection.

The whole-cell potassium currents were recorded using an EPC10-USB amplifier with Patchmaster software v2*73.5 (HEKA Elektronic), sampled at 10 kHz and filtered at 2.9 kHz (low-pass Bessel). The external solution contained (in mM) 140 NaCl, 5 KCl, 1 $MgCl_2$, 2 $CaCl_2$, 10 Glucose, and 10 HEPES (pH 7.4). The internal solution contained (in mM) 145 KCl, 10 HEPES, 5 EGTA, and 2 Mg-ATP (pH 7.4). Borosilicate pipette electrodes (Sutter Instrument) with a resistance of 2–4 MΩ were used.

To obtain the voltage-dependent activation curves, cells were stepped from a −80 mV holding potential to voltages ranging from −90 mV to +70 mV for 1,500 ms in 10 mV increments. Tail currents were then recorded at −120 mV for 500 ms. Only cells with series resistance < 10 MΩ were included, and series resistance compensation was set to > 90%. Tail peak currents were measured to reflect conductance (G) at different applied voltage steps. Conductance activation curves were fitted to a Boltzmann equation: $G/G_{max} = 1/\{1 + \exp[(V_{1/2} - V_m)/slope]\}$, where G_{max} is the maximal conductance, $V_{1/2}$ is the half-activation potential, V_m is the membrane potential, and slope is the slope factor.

For assessing the effects of ICA-110381 and XEN1101, cells were stepped from a −100 mV holding potential to voltages ranging from −110 mV to +50 mV for 1,500 ms in 10 mV increments. Tail currents were then recorded at −120 mV for 500 ms. During the experiments, the bath solution was continuously perfused by a gravity-perfusion system (ALA Scientific Instruments), and the compound solutions were perfused for several minutes to achieve steady effects. Concentration-response curves were fitted using the equation Y = Bottom + (Top − Bottom) / (1 + 10^((LogEC_{50}-X) * Hill Slope)), where Y represents the shifts of $V_{1/2}$ of the Boltzmann relationship for the voltage-dependent activation induced by different compound concentrations, EC_{50} is the concentration of the compound that activated 50% of the max change in $V_{1/2}$ and X denoted the log of concentration, and Hill Slope indicated the slope factor. The effect of ICA-110381 on KCNQ2, KCNQ3, and KCNQ2/3 was quantified by the shifts in $V_{1/2}$ at 10 μM, respectively.

To evaluate the conductivity of different modified proteins, current density was calculated by measuring tail peak currents in response to +50 mV voltage steps, followed by normalization to cell capacitance (pA/pF).

Data were analyzed using Fitmaster (HEKA Elektronik), Origin (OriginLab), and GraphPad Prism (GraphPad Software). All data points are presented as mean ± SEM, with *n* indicating the number of experimental cells. Statistical significance was assessed using unpaired *t*-tests, one-way ANOVA analysis, and extra sum-of-squares F tests.

DATA AVAILABILITY

The data that support this study are available from the corresponding authors upon reasonable request. The cryo-EM maps and corresponding atomic models have been deposited in the Electron Microscopy Data Bank (EMDB) and the Protein Data Bank (PDB) under the following accession codes: homomeric KCNQ2 in *apo* state (EMD-68141, 22AY), KCNQ2/KCNQ3 with 3:1 stoichiometry in *apo* state (EMD-68152, 22BJ), KCNQ2/KCNQ3 with 2:2 stoichiometry in *apo* state (EMD-68153, 22BK), ICA-110381-bound KCNQ2/KCNQ3 with 3:1 stoichiometry, state-1 (EMD-68142, 22AZ), ICA-110381-bound KCNQ2/KCNQ3 with 3:1 stoichiometry, state-2 (EMD-68143, 22BA), ICA-110381-bound KCNQ2/KCNQ3 with 3:1 stoichiometry, state-3 (EMD-68145, 22BC), ICA-110381-bound KCNQ2/KCNQ3 with 2:2 stoichiometry (EMD-68146, 22BD), XEN1101-bound KCNQ2/KCNQ3 with 3:1 stoichiometry, state-1 (EMD-68147, 22BE), XEN1101-bound KCNQ2/KCNQ3 with 3:1 stoichiometry, state-2 (EMD-68148, 22BF), XEN1101-bound KCNQ2/KCNQ3 with 3:1 stoichiometry, state-3 (EMD-68149, 22BG), XEN1101-bound KCNQ2/KCNQ3 with 3:1 stoichiometry, state-4 (EMD-68150, 22BH), XEN1101-bound KCNQ2/KCNQ3 with 2:2 stoichiometry (EMD-68151, 22BI). The cryo-EM maps of XEN1101-bound KCNQ2/KCNQ3 co-expressed with CaM were used to confirm the stoichiometries and conformational states without model building. The related maps have been deposited as EMD-80883 (XEN1101-bound KCNQ2/KCNQ3-CaM with 3:1 stoichiometry, state-1), EMD-80884 (XEN1101-bound KCNQ2/KCNQ3-CaM with 3:1 stoichiometry, state-2), EMD-80885 (XEN1101-bound KCNQ2/KCNQ3-CaM with 3:1 stoichiometry, state-3), EMD-80886 (XEN1101-bound KCNQ2/KCNQ3-CaM with 3:1 stoichiometry, state-4), and EMD-80887 (XEN1101-bound KCNQ2/KCNQ3-CaM with 2:2 stoichiometry), respectively.

ACKNOWLEDGMENTS

We thank the Structural Biology and Biomedical Electrophysiology Core Facilities at the Bio-Tech Center, as well as the Computing Labware for Electron-microscopy Visualization and Experimental Research (CLEVER) at the Biomedical Data Center, of Shenzhen Medical Academy of Research and Translation (SMART) for their technical support and experimental assistance. We are grateful to Dr. Kun Wu at the SMART-SZBL Rare Disease Center for providing information on KCNQ-related disease mutations. This work was funded by the National Natural Science Foundation of China (32501082 to J.H.) and the Guangdong Pearl River Talent Program (ZJQNRC20241219163128017 to J.H.). J.H. and X.F. are also supported by the start-up funding from Shenzhen Medical Academy of Research and Translation (SMART).

AUTHOR CONTRIBUTIONS

J.H. conceived the project. F.L., X.H., G.C., X.S., Y.X., P.H., F.Y., X.F., and J.H. designed experiments; F.L., X.H., Y.X., and F.Y. carried out experiments related to cryo-EM studies, including protein expression, purification, and data acquisition; X.F. and J.H. performed data processing; G.C. conducted experiments related to electrophysiology; F.L., X.S., and P.H. prepared the plasmids for electrophysiological analyses; F.L., X.H., G.C., X.S., Y.X., P.H., F.Y., X.F., and J.H. analyzed data; F.L., X.H., X.F., and J.H. wrote the manuscript with input from all authors. All authors approved the final manuscript.

COMPETING INTERESTS

The authors declare no competing interests.

REFERENCES

1. Barrese, V., Stott, J.B. & Greenwood, I.A. KCNQ-encoded potassium channels as therapeutic targets. *Annu. Rev. Pharmacol. Toxicol.* **58**, 625–648 (2018).
2. Abbott, G.W. KCNQs: ligand- and voltage-gated potassium channels. *Front. Physiol.* **11**, 583 (2020).
3. Cooper, E.C. & Jan, L.Y. M-channels: neurological diseases, neuromodulation, and drug development. *Arch. Neurol.* **60**, 496–500 (2003).
4. Agsten, M. et al. BACE1 modulates gating of KCNQ1 (Kv7.1) and cardiac delayed rectifier KCNQ1/KCNE1 (I_{Ks}). *J. Mol. Cell. Cardiol.* **89**, 335–348 (2015).
5. Kubisch, C. et al. KCNQ4, a novel potassium channel expressed in sensory outer hair cells, is mutated in dominant deafness. *Cell* **96**, 437–446 (1999).
6. Kharkovets, T. et al. KCNQ4, a K^+ channel mutated in a form of dominant deafness, is expressed in the inner ear and the central auditory pathway. *Proc. Natl. Acad. Sci. USA* **97**, 4333–4338 (2000).
7. Brown, D.A. & Adams, P.R. Muscarinic suppression of a novel voltage-sensitive K^+ current in a vertebrate neurone. *Nature* **283**, 673–676 (1980).
8. Jentsch, T.J. Neuronal KCNQ potassium channels: physiology and role in disease. *Nat. Rev. Neurosci.* **1**, 21–30 (2000).
9. Wang, J.J. & Li, Y. KCNQ potassium channels in sensory system and neural

circuits. *Acta Pharmacol. Sin.* **37**, 25–33 (2016).

10. Wang, H.S. et al. KCNQ2 and KCNQ3 potassium channel subunits: molecular correlates of the M-channel. *Science* **282**, 1890–1893 (1998).
11. Devaux, J.J., Kleopa, K.A., Cooper, E.C. & Scherer, S.S. KCNQ2 is a nodal K^+ channel. *J. Neurosci.* **24**, 1236–1244 (2004).
12. Etxeberria, A., Santana-Castro, I., Regalado, M.P., Aivar, P. & Villarroel, A. Three mechanisms underlie KCNQ2/3 heteromeric potassium M-channel potentiation. *J. Neurosci.* **24**, 9146–9152 (2004).
13. Bal, M., Zhang, J., Zaika, O., Hernandez, C.C. & Shapiro, M.S. Homomeric and heteromeric assembly of KCNQ (Kv7) K^+ channels assayed by total internal reflection fluorescence/fluorescence resonance energy transfer and patch clamp analysis. *J. Biol. Chem.* **283**, 30668–30676 (2008).
14. Soh, H., Springer, K., Doci, K., Balsbaugh, J.L. & Tzingounis, A.V. KCNQ2 and KCNQ5 form heteromeric channels independent of KCNQ3. *Proc. Natl. Acad. Sci. USA* **119**, e2117640119 (2022).
15. Varghese, N. et al. KCNQ2/3 Gain-of-function variants and cell excitability: differential effects in CA1 versus L2/3 pyramidal neurons. *J. Neurosci.* **43**, 6479–6494 (2023).
16. Doyle, D.A. et al. The structure of the potassium channel: molecular basis of K^+ conduction and selectivity. *Science* **280**, 69–77 (1998).
17. Sun, J. & MacKinnon, R. Cryo-EM structure of a KCNQ1/CaM complex reveals insights into congenital long QT syndrome. *Cell* **169**, 1042–1050.e9 (2017).
18. Wu, X.A., Perez, M.E., Noskov, S.Y. & Larsson, H.P. A general mechanism of KCNE1 modulation of KCNQ1 channels involving non-canonical VSD-PD coupling. *Commun. Biol.* **4**, 887 (2021).
19. Huang, J., Pan, X.J. & Yan, N.E. Structural biology and molecular pharmacology of voltage-gated ion channels. *Nat. Rev. Mol. Cell Biol.* **25**, 904–925 (2024).
20. Sun, J. & MacKinnon, R. Structural basis of human KCNQ1 modulation and gating. *Cell* **180**, 340–347.e9 (2020).
21. Li, T. et al. Structural basis for the modulation of human KCNQ4 by small-molecule drugs. *Mol. Cell* **81**, 25–37.e4 (2021).
22. Li, X.X. et al. Molecular basis for ligand activation of the human KCNQ2 channel. *Cell Res.* **31**, 52–61 (2021).
23. Zheng, Y. et al. Structural insights into the lipid and ligand regulation of a human neuronal KCNQ channel. *Neuron* **110**, 237–247.e4 (2022).
24. Ma, D.M. et al. Ligand activation mechanisms of human KCNQ2 channel. *Nat. Commun.* **14**, 6632 (2023).
25. Zhang, S.Y. et al. A small-molecule activation mechanism that directly opens the KCNQ2 channel. *Nat. Chem. Biol.* **20**, 847–856 (2024).
26. Li, J.N. et al. Small molecule inhibits KCNQ channels with a non-blocking mechanism. *Nat. Chem. Biol.* **21**, 1100–1109 (2025).
27. Yang, Z.N. et al. Phosphatidylinositol 4,5-bisphosphate activation mechanism of human KCNQ5. *Proc. Natl. Acad. Sci. U. S. A.* **122**, e2416738122 (2025).
28. Kasuya, G. & Nakajo, K. Optimized tight binding between the S1 segment and KCNE3 is required for the constitutively open nature of the KCNQ1-KCNE3 channel complex. *Elife* **11**, e81683 (2022).
29. Cui, C.X. et al. Mechanisms of KCNQ1 gating modulation by KCNE1/3 for cell-specific function. *Cell Res.* **35**, 876–886 (2025).
30. Ambrosino, P. et al. Epilepsy-causing mutations in Kv7.2 C-terminus affect binding and functional modulation by calmodulin. *Biochim. Biophys. Acta* **1852**, 1856–1866 (2015).
31. Bernardo-Seisdedos, G. et al. Structural basis and energy landscape for the Ca^{2+} gating and calmodulation of the Kv7.2 K^+ channel. *Proc. Natl. Acad. Sci. USA* **115**, 2395–2400 (2018).
32. Chang, A. et al. A Calmodulin C-lobe Ca^{2+}-dependent switch governs Kv7 channel function. *Neuron* **97**, 836–852.e6 (2018).
33. Zaydman, M.A. & Cui, J.M. PIP_2 regulation of KCNQ channels: biophysical and molecular mechanisms for lipid modulation of voltage-dependent gating. *Front. Physiol.* **5**, 195 (2014).
34. Choveau, F.S., De la Rosa, V., Bierbower, S.M., Hernandez, C.C. & Shapiro, M.S. Phosphatidylinositol 4,5-bisphosphate (PIP_2) regulates KCNQ3 K^+ channels by interacting with four cytoplasmic channel domains. *J. Biol. Chem.* **293**, 19411–19428 (2018).
35. Brueggemann, L.I., Mackie, A.R., Martin, J.L., Cribbs, L.L. & Byron, K.L. Diclofenac distinguishes among homomeric and heteromeric potassium channels composed of KCNQ4 and KCNQ5 subunits. *Mol. Pharmacol.* **79**, 10–23 (2011).
36. Nissenkorn, A. et al. Donepezil as a new therapeutic potential in KCNQ2- and KCNQ3-related autism. *Front. Cell. Neurosci.* **18**, 1380442 (2024).
37. Schubert-Bast, S. et al. Sodium channel blockers in KCNQ2-encephalopathy: lacosamide as a new treatment option. *Seizure* **51**, 171–173 (2017).
38. Goto, A. et al. Characteristics of *KCNQ2* variants causing either benign neonatal epilepsy or developmental and epileptic encephalopathy. *Epilepsia* **60**, 1870–1880 (2019).
39. Biervert, C. et al. A potassium channel mutation in neonatal human epilepsy. *Science* **279**, 403–406 (1998).
40. Singh, N.A. et al. A novel potassium channel gene, *KCNQ2*, is mutated in an inherited epilepsy of newborns. *Nat. Genet.* **18**, 25–29 (1998).
41. Allen, N.M. et al. The variable phenotypes of KCNQ-related epilepsy. *Epilepsia* **55**, e99–e105 (2014).
42. Allen, N.M., Weckhuysen, S., Gorman, K., King, M.D. & Lerche, H. Genetic potassium channel-associated epilepsies: clinical review of the K_v family. *Eur. J. Paediatr. Neurol.* **24**, 105–116 (2020).
43. Vanoye, C.G. et al. High-throughput evaluation of epilepsy-associated *KCNQ2* variants reveals functional and pharmacological heterogeneity. *JCI Insight* **7**, e156314 (2022).
44. Beacher, N.G., Brodie, M.J. & Goodall, C. A case report: retigabine induced oral mucosal dyspigmentation of the hard palate. *BMC Oral Health* **15**, 122 (2015).
45. Clark, S., Antell, A. & Kaufman, K. New antiepileptic medication linked to blue discoloration of the skin and eyes. *Ther. Adv. Drug Saf.* **6**, 15–19 (2015).
46. Namdari, R., Luzon, C., Cadieux, J.A., Leung, J. & Beatch, G.N. Pharmacokinetics of XEN496, a novel pediatric formulation of Ezogabine, under fed and fasted conditions: a phase 1 trial. *Neurol. Ther.* **11**, 781–796 (2022).
47. Groseclose, M.R. & Castellino, S. An investigation into Retigabine (Ezogabine) associated dyspigmentation in rat eyes by MALDI imaging mass spectrometry. *Chem. Res. Toxicol.* **32**, 294–303 (2019).
48. Brickel, N., Gandhi, P., VanLandingham, K., Hammond, J. & DeRossett, S. The urinary safety profile and secondary renal effects of retigabine (ezogabine): a first-in-class antiepileptic drug that targets KCNQ (K_v7) potassium channels. *Epilepsia* **53**, 606–612 (2012).
49. Svalø, J., Sheykhzade, M., Nordling, J., Matras, C. & Bouchelouche, P. Functional and molecular evidence for K_v7 channel subtypes in human detrusor from patients with and without bladder outflow obstruction. *PLoS One* **10**, e0117350 (2015).
50. French, J.A. et al. Efficacy and safety of XEN1101, a novel potassium channel opener, in adults with focal epilepsy: a phase 2b randomized clinical trial. *JAMA Neurol.* **80**, 1145–1154 (2023).
51. Yang, G.M. et al. Functional characterization and in vitro pharmacological rescue of KCNQ2 pore mutations associated with epileptic encephalopathy. *Acta Pharmacol. Sin.* **44**, 1589–1599 (2023).
52. Lattanzi, S. et al. A profile of azetukalner for the treatment of epilepsy: from pharmacology to potential for therapy. *Expert Rev. Clin. Pharmacol.* **17**, 423–432 (2024).
53. Boehlen, A. et al. The new KCNQ2 activator 4-Chlor-N-(6-chlor-pyridin-3-yl)-benzamid displays anticonvulsant potential. *Br. J. Pharmacol.* **168**, 1182–1200 (2013).
54. Filareto, I. et al. Pharmacological approaches in drug-resistant pediatric epilepsies caused by pathogenic variants in potassium channel genes. *Front. Cell. Neurosci.* **18**, 1512365 (2025).
55. Schwake, M., Jentsch, T.J. & Friedrich, T. A carboxy-terminal domain determines the subunit specificity of KCNQ K^+ channel assembly. *EMBO Rep.* **4**, 76–81 (2003).
56. Schwake, M. et al. Structural determinants of M-type KCNQ (K_v7) K^+ channel assembly. *J. Neurosci.* **26**, 3757–3766 (2006).

57. Gomez-Posada, J.C. et al. A pore residue of the KCNQ3 potassium M-channel subunit controls surface expression. *J. Neurosci.* **30**, 9316–9323 (2010).
58. Zaika, O., Hernandez, C.C., Bal, M., Tolstykh, G.P. & Shapiro, M.S. Determinants within the turret and pore-loop domains of KCNQ3 K^+ channels governing functional activity. *Biophys. J.* **95**, 5121–5137 (2008).
59. Whiffin, N. et al. CardioClassifier: disease- and gene-specific computational decision support for clinical genome interpretation. *Genet. Med.* **20**, 1246–1254 (2018).
60. Martin, H.C. et al. Clinical whole-genome sequencing in severe early-onset epilepsy reveals new genes and improves molecular diagnosis. *Hum. Mol. Genet.* **23**, 3200–3211 (2014).
61. Tatulian, L., Delmas, P., Abogadie, F.C. & Brown, D.A. Activation of expressed KCNQ potassium currents and native neuronal M-type potassium currents by the anti-convulsant drug retigabine. *J. Neurosci.* **21**, 5535–5545 (2001).
62. Kim, K.S., Duignan, K.M., Hawryluk, J.M., Soh, H. & Tzingounis, A.V. The voltage activation of cortical KCNQ channels depends on global PIP2 levels. *Biophys. J.* **110**, 1089–1098 (2016).
63. Bialer, M. et al. Progress report on new antiepileptic drugs: a summary of the sixteenth Eilat conference on new antiepileptic drugs and devices (EILAT XVI): II. Drugs in more advanced clinical development. *Epilepsia* **63**, 2883–2910 (2022).
64. Punjani, A., Rubinstein, J.L., Fleet, D.J. & Brubaker, M.A. cryoSPARC: algorithms for rapid unsupervised cryo-EM structure determination. *Nat. Methods* **14**, 290–296 (2017).
65. Bepler, T. et al. Positive-unlabeled convolutional neural networks for particle picking in cryo-electron micrographs. *Nat. Methods* **16**, 1153–1160 (2019).
66. Emsley, P., Lohkamp, B., Scott, W.G. & Cowtan, K. Features and development of *Coot*. *Acta Crystallogr. D Biol. Crystallogr.* **66**, 486–501 (2010).
67. Afonine, P.V. et al. Towards automated crystallographic structure refinement with *phenix.refine*. *Acta Crystallogr. D Biol. Crystallogr.* **68**, 352–367 (2012).
68. Croll, T.I. *ISOLDE*: a physically realistic environment for model building into low-resolution electron-density maps. *Acta Crystallogr. D Struct. Biol.* **74**, 519–530 (2018).
69. Pettersen, E.F. et al. UCSF ChimeraX: structure visualization for researchers, educators, and developers. *Protein Sci.* **30**, 70–82 (2021).

ADDITIONAL INFORMATION

Supplementary information The online version contains supplementary material available at https://doi.org/10.15302/vita.2026.05.0035.

Correspondence and requests for materials should be addressed to Jian Huang, or Xiao Fan.

Reprints and permission information is available at https://www.vita-journal.com/.